Journal of Electromagnetic Waves and Applications, Vol. 14, 1637–1667, 2000

VALIDATION OF 2D INVERSE SCATTERING ALGORITHMS FROM MULTI-FREQUENCY EXPERIMENTAL DATA

K. Belkebir, S. Bonnard, F. Pezin, P. Sabouroux, and M. Saillard

Institut Fresnel, UMR CNRS
Campus de Saint Jérôme, case 162
13397 Marseille CEDEX 20, France

Abstract–Reconstructions of two dimensional dielectric or conducting objects from multi-frequency experimental data are considered in the present paper. Two different iterative methods are used for solving the inverse scattering problem. The first one is based on a boundary integral formalism and retrieves boundaries and complex permittivities of unknown homogeneous scatterers. For this method initial guesses are derived from method of decomposition of the time reversal operator (DORT) combined with a low frequency approximation. The second method is based on a domain integral formalism and retrieves the relative complex permittivity distribution inside some investigated domain. The data were carried out in a controlled environment (anechoic chamber) and the reconstructions have been performed using multi-frequency approach, i.e., the scheme starts with the lowest available frequency and uses the final result as initial guess at higher frequency in order to enhance the resolution.

1. INTRODUCTION

The present paper deals with the reconstruction, from a measured scattered field, of the shape and of electromagnetic parameters of unknown objects illuminated by a known electromagnetic excitation. During the last decade the development of algorithms for solving such inverse scattering problem has gained much interest. There are several ways to tackle the problem depending on the application at hand and on the realistic assumptions to be made. For example, a quasi-real time reconstruction can be reached with algorithms based on diffraction to-

mography [1, 2] but the price to be paid is that the reconstruction is merely qualitative in the sense that only the induced current density distribution is retrieved. Another approach for solving the inverse scattering problem is the use of iterative methods [3–7] which, starting from an initial guess of the parameter of interest, adjust step by step the unknown by minimizing an adequate cost function related to the discrepancy between the data and those that would be generated with the estimated parameter. When dealing with synthetic data, some care has to be taken to avoid an inverse crime, which is described in [8] as occurring when the forward solver used to generate the data is also used in the inversion procedure, or when the same discretization is used in both numerical procedures. An obvious step is to validate the inversion algorithms with real data obtained in a controlled environment. This might be an intermediary step, before applying inverse algorithms to a realistic configuration which is always extremely complicated. The Ipswich data base is available for teams developing algorithms to solve the inverse scattering problem. Results have been obtained with different methods including: (i) diffraction tomography, (ii) linearized methods such as the distorted wave Born method or Newton-Kantorovich algorithm, (iii) the modified gradient and its variant the contrast source inversion method. These results are reported in [9–15] for the first set corresponding to simple shaped objects. For more complicated objects, the results are presented in [16–23] and [24–31] for the second and third set, respectively. The experimental setup is described in [9] and the measured data were provided courtesy of Rome Laboratory Electromagnetic Measurement Facility, in Ipswich, Massachusetts. The data consist in a measured scattered far field for a single frequency with several angles of incidence.

In order to enlarge the scope of applications and inspired by the Ipswich sessions, we carried out a series of experiments in the anechoic chamber of the *Center Commun de Resources Micro-ondes* (CCRM) in Marseille. This facility has been designed for three-dimensional bistatic measurements, thanks to three angular degrees of freedom. Therefore, most configurations encountered in applications can be reproduced, for instance a fixed transmitter with a mobile receiver, or a transmitter and a receiver moving together, or both moving independently. We used the latter configuration, with two degrees of freedom only, since the study is restricted to cylindrical objects. Indeed, the algorithms tested here are based on rigorous integral formalisms, and lead to iterative processes

with the aim of minimizing a cost function. One of them, based on the modified gradient method [6, 32], can deal with a large variety of problems, involving inhomogeneous and large contrasted objects. As a counterpart, this algorithm is numerically expensive, thus has been developed for two-dimensional problems first.

The reconstruction can be speeded up with the help of additional assumptions. For instance, it is well known that, for low contrasts between the scatterer and the embedding medium, the Born approximation makes the inverse scattering problem linear and its solution can be obtained rapidly. Here, we have tested a method restricted to homogeneous objects, with arbitrary contrasts. In this case, the domain integral equations can be replaced by boundary equations, involving much less unknowns. The generalization of this method to three-dimensional inverse problems would not require large numerical facilities. In order to validate both domain and boundary integral methods, the reconstructions from real data performed in this paper only concern homogeneous objects, either dielectric or metallic.

The cost functions often present local minima, and methods to avoid being trapped in them are generally time consuming [33]. To overcome this problem, a multiple frequency approach has been implemented [34, 35], i.e., the iterative scheme is started at low frequency and the final result is used as initial guess at higher frequency in order to enhance the resolution. Indeed, it has been observed that local minima are avoided at low frequencies thanks to the accuracy of the initial guess derived from an approximate theory, and that convergence is more easily and rapidly achieved. Since the frequency of the experimental setup is tunable from 1 to 18 GHz, multi-frequency data have thus been recorded between 1 and 8 or between 2 and 16 GHz, depending on the size of the scatterer.

How to model the incident field is another important issue when dealing with real data. The difficulty is reinforced when the algorithm is restricted to two-dimensional geometries, where the field emitted by the horn antenna must be represented by a cylindrical wave. From measurements without any scatterer and from far-field approximations, an estimation of the value and of the polarization of the incident field has been derived in the target area. For reconstruction purposes, this estimated field is approached with the help of fictitious wire antennas.

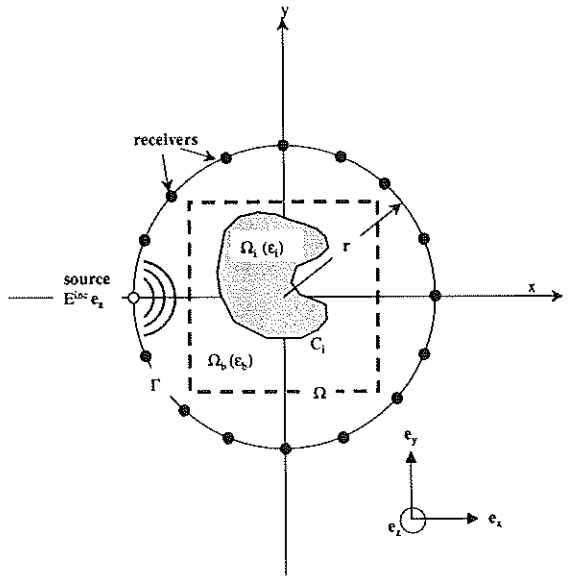

Figure 1. Geometry of the problem.

2. NOTATIONS AND STATEMENT OF THE PROBLEM

The geometry of the problem studied in this paper is depicted in Fig. 1 where a two-dimensional object of cross-section Ω_i with arbitrary boundary C_i is confined in a domain Ω. The embedding medium Ω_b is assumed to be infinite and homogeneous, with permittivity $\varepsilon_b = \varepsilon_0 \varepsilon_{rb}$, and permeability $\mu = \mu_0$. The scatterers are assumed to be homogeneous cylinders when dealing with boundary integral formalism and inhomogeneous when dealing with domain integral formalism. The permittivity of the scatterers is denoted by $\varepsilon_i = \varepsilon_0 \varepsilon_{ri}$ and the permeability $\mu_i = \mu_0$.

A right-handed Cartesian coordinate frame $(O, \mathbf{e_x}, \mathbf{e_y}, \mathbf{e_z})$ is defined. The origin O could be either inside or outside the scatterer and the z-axis is parallel to the axis of the scatterer. When needed, cylindrical coordinates (ρ, θ, z) are also used and the position vector OM is written as:

$$OM = x\,\mathbf{e_x} + y\,\mathbf{e_y} + z\,\mathbf{e_z} = \mathbf{r} + z\,\mathbf{e_z}. \tag{1}$$

The unit normal vector $\mathbf{n}$ to the scatterer is directed outwards the cylinder and the unit tangential vector is defined by: $\mathbf{t} = \mathbf{n} \times \mathbf{e_z}$.

The sources are assumed to be lines parallel to the z-axis, located at $(\mathbf{r}_l)_{1\leq l\leq L}$. Therefore, the diffraction problem can be reduced to a two-dimensional one with two fundamental cases of polarization: the $E_{//}$ case and the $H_{//}$ case depending on whether the electric field or the magnetic field is parallel to the z-axis respectively. Taking into account a time dependence in $\exp(-j\omega t)$, in the $E_{//}$ case the time-harmonic incident electric field created by the lth line source is:

$$\mathbf{E}_l^{inc}(\mathbf{r}) = E_l^{inc}(\mathbf{r})\mathbf{e}_z = P\mathbf{e}_z \frac{\omega\mu_0}{4} H_0^{(1)}\left(k_b\left|\mathbf{r}-\mathbf{r}_l\right|\right), \tag{2}$$

where P is the strength of the electric source, ω the angular frequency, $H_0^{(1)}$ the Hankel function of zero order and first kind, k_b the wavenumber in the surrounding medium.

For the inverse scattering problem we restrict the study to the $E_{//}$ polarization and we assume that the unknown object is successively illuminated by $l = 1, \ldots, L$ electromagnetic excitations and for each incident field the scattered field is available along a surface Γ at M positions.

3. INVERSION ALGORITHM BASED ON BOUNDARY INTEGRAL FORMALISM

3.1 Integral Equation

For the sake of simplicity, the equations are established with one cylinder, but the generalization to several cylinders is straightforward. The forward two-dimensional problem is solved using a boundary integral equation, based on a single layer representation of the scattered field $E^d = E - E^{inc}$, with density ϕ:

$$E^d(\mathbf{r}) = \int_{C_i} G(\mathbf{r},\mathbf{r}')\phi(\mathbf{r}')ds'. \tag{3}$$

where G is the 2D free-space Green function $G(\mathbf{r},\mathbf{r}') = -\frac{j}{4}H_0^{(1)}(k_b|\mathbf{r}-\mathbf{r}'|)$. The unknown surface density ϕ satisfies the boundary integral equation written in the operator form [36]:

$$\mathbf{A}\phi = B \tag{4}$$

where, identifying the integral operators and their kernel,

$$\mathbf{A} = \left(\frac{\delta}{2} - \frac{dG_i}{dn'}\right).G + G_i.\left(\frac{\delta}{2} + \frac{dG}{dn}\right) \tag{5}$$

$$B = -\left(\frac{\delta}{2} - \frac{dG_i}{dn'}\right)E^i - G_i\frac{dE^i}{dn} \tag{6}$$

with

- G_i defined as G but with the wavenumber k_i,
- $\frac{dG}{dn}$ being the normal derivative evaluated at $\mathbf{r}$,
- $\frac{dG_i}{dn'}$ being the normal derivative evaluated at $\mathbf{r}'$.

The integral equation is transformed into a linear system using a boundary finite element method. The boundary $\mathcal{C}_i$ is represented by a polygonal contour with N segments. The result is a dense linear system of N equations solved by a classical LU decomposition. For typical examples, N ranges from 50 to 100.

3.2 Cost Functional

The aim of the computation is to determine the shape $\mathcal{C}_i$ and the permittivity ε_i of the diffracting cylinder from the knowledge of the permittivity of the embedding medium ε_b, the incident fields $\left(E_l^{inc}\right)_l$ and the set of $L \times M$ measured fields $f_{l,m}$. The shape and the permittivity are alternatively estimated in an iterative scheme, in order to minimize a cost functional which gives the normalized deviation between the computed field and the measured one. This cost functional is defined by:

$$F(\mathcal{C}_i, \varepsilon_i) = \frac{1}{L \times M}\sum_{l=1}^{L}\sum_{m=1}^{M}\frac{\left|E_l^d(\mathbf{r}_m) - f_{l,m}\right|^2}{\left|f_{l,m}\right|^2} \tag{7}$$

where, for a given receiving antenna located at $\mathbf{r}_m$ and a given incident field E_l^{inc},

- $f_{l,m}$ is the measured scattered field,
- $E_l^d(\mathbf{r}_m)$ is the field scattered by an object with boundary $\mathcal{C}_i$ and permittivity ε_i.

3.3 Shape Reconstruction

The minimization of the above cost functional is performed by a conjugate gradient method with linear search of the minimum in the

conjugate direction. In order to find a new shape at each step of the iterative algorithm, the functional derivative of F is needed. If δE^d is a given change in the computed field, a simple differentiation yields:

$$\delta F = \frac{2}{L \times M} \sum_{l=1}^{L} \sum_{m=1}^{M} \Re e \left[\overline{\left(\frac{E_l^d(\mathbf{r}_m) - f_{l,m}}{f_{l,m}} \right)} \frac{\delta E_l^d(\mathbf{r}_m)}{f_{l,m}} \right], \quad (8)$$

where the overbar denotes complex conjugation.

The adjoint state method [37, 38], based on the Lorentz reciprocity theorem, is used here to calculate the variation of the electric field δE as a function of a small change δC_i of the shape C_i. It is shown that the functional derivative can be written as a simple boundary integral of the solution of two adjoint diffraction problems:

$$\delta E_l(\mathbf{r}_m) \simeq j\omega(\varepsilon_i - \varepsilon_b) \int_{C_i} E_l . E_l^a \delta C_i \, ds. \quad (9)$$

where E_l^a denotes the electric field obtained when the line source is located at the observation point $\mathbf{r_m}$.

3.4 Determination of Permittivities

The determination of the permittivity ε_i is also achieved by minimizing the cost functional described in Section 3.2, with the same conjugate gradient method. The profile C_i of the cylinder is fixed and the aim is to compute the gradient of the cost functional with respect to the permittivity ε_i. From the definition of the wavenumber k_i and the properties of derivation of composed functions, we have:

$$\frac{\delta F}{\delta \varepsilon_i} = \frac{\delta k_i}{\delta \varepsilon_i} \frac{\delta F}{\delta k_i} = \frac{k_i}{2\varepsilon_i} \frac{\delta F}{\delta k_i} \quad (10)$$

In order to compute $\frac{\delta F}{\delta k_i}$, the expression (8) shows that computation of $\frac{\delta E^d}{\delta k_i}$ is needed. Starting from (3), we derive:

$$\frac{\delta E^d}{\delta k_i}(\mathbf{r}) = \int_{C_i} G(\mathbf{r}, \mathbf{r}') \frac{\delta \phi}{\delta k_i}(\mathbf{r}') \, ds' = \mathbf{G} \frac{\delta \phi}{\delta k_i}, \quad (11)$$

Note that $\frac{\delta E^d}{\delta k_i} = \frac{\delta E}{\delta k_i}$ because the incident field is independant of k_i. Now, to evaluate $\frac{\delta \phi}{\delta k_i}$, we have to solve the integral equation obtained

by taking the derivative of (4) with respect to the wavenumber k_i. This yields:

$$\mathbf{A}\frac{\delta\phi}{\delta \mathrm{k_i}} = \frac{\delta \mathbf{B}}{\delta \mathrm{k_i}} - \frac{\delta \mathbf{A}}{\delta \mathrm{k_i}}\phi. \tag{12}$$

It results that here also, the derivative is obtained by solving two linear systems with the same matrix, representing the integral operator $\mathbf{A}$.

3.5 Initial Guess

Our iterative scheme requires some initialization which, in general, cannot be arbitrary. Indeed, since the cost function may have local minima, one must start as "close" as possible to the solution. In addition, since we have not been able to build a rather systematic and reliable criterion to split or to coalesce the various boundaries during the reconstruction process, the number of scatterers in the investigated area must be known. To overcome this problem, we first attempt to derive the number of scatterers and their location directly from the data. With this aim, we apply the so-called decomposition of the time reversal operator (DORT) method [39]. The principle is as follows: for each source radiating alone, M values of the scattered field are recorded by the receivers. This way, a M by L matrix $\mathbf{T}$ is built. Since here time reversal and phase conjugation are equivalent [40], the combination of the direct and of the time-reversed scattering events is thus described by $\mathbf{H} = \mathbf{T}^*\mathbf{T}$, where $\mathbf{T}^*$ denotes the adjoint of $\mathbf{T}$, and $\mathbf{H}$ represents the so-called time reversal operator.

The properties of the time reversal operator in the frame of a rigorous electromagnetic theory have been extensively studied in a recent paper [41] For a single cylindrical scatterer in the low frequency range, the eigenvalues distribution follows that of the coefficients of the Fourier-Bessel expansion of the scattered field. Therefore, in s polarization, provided that the size of the scatterer does not exceed half a wavelength, the zero order term strongly dominates. Consequently, the associated eigenvalue remains much larger than the others. Since this term describes the isotropic part of the radiated field, the corresponding eigenvector provides the distribution of the L complex amplitudes allowing one to synthesize a cylindrical wave focusing onto the scatterer from L line sources placed at $(\mathbf{r}_m)_m$. This method is very efficient to get an accurate estimation of the location of a scatterer. In addition, it is very robust against noise, as can be predicted from the capacity of phase conjugation mirrors to compensate wave front perturbations

during the backpropagation. When several objects are present, their number can be easily deduced from the eigenvalues distribution if their scattering cross-sections are comparable. The behavior of the eigenvectors may be less obvious, but some means to obtain the location of the objects have been suggested in [41]. Concerning permittivity, though approximate methods could provide some estimation, it is arbitrary set to the one of the surrounding medium.

3.6 Regularization

In the shape reconstruction process, the conjugate gradient algorithm minimizes the cost functional F by computing the displacement $\delta \mathbf{M}_n$ of the middle of each segment along the normal. At each step of the iteration, it gives us the new middles from which the position of the new vertices are determined. A drawback is to take N as an odd number. Besides, we have noticed that the reconstructed profile becomes very irregular after just a few iterations. To overcome this problem, we propose a regularization based on a new representation of the profile as a Fourier series.

Numerically, the regularization procedure is as follows: starting from a circular profile, parameterized by the function $C(\theta) = a_0 + a_1 \exp(j\theta)$, our iterative process computes $\frac{\delta F}{\delta a_0}$ and $\frac{\delta F}{\delta a_1}$ in order to find the optimal coefficients a_0 and a_1 which represent the center and the radius respectively. The profile obtained is called "optimal circle". Then, the coefficient a_{-1} is inserted and the function becomes $C(\theta) = a_0 + a_1 \exp(j\theta) + a_{-1} \exp(-j\theta)$. The initial values a_0 and a_1 are those found for the "optimal circle" and $a_{-1} = 0$. As previously, we search for the optimal coefficients a_0, a_1, and a_{-1} by computing $\frac{\delta F}{\delta a_0}$, $\frac{\delta F}{\delta a_1}$, and $\frac{\delta F}{\delta a_{-1}}$ to obtain the "optimal ellipse". Afterwards, we repeat the same process with more and more Fourier coefficients.

4. INVERSION ALGORITHM BASED ON DOMAIN INTEGRAL FORMALISM

4.1 Principles of the Algorithm

The direct scattering problem may be formulated as two contrast-source integral relations (i) the state or observation equation and (ii) the field or coupling equation

$$E_l^d(\mathbf{r} \in \Gamma) = \int_\Omega k_0^2 \chi(\mathbf{r}') E_l(\mathbf{r}') G(\mathbf{r}, \prime) d\mathbf{r}', \tag{13}$$

$$E_l(\mathbf{r} \in \Omega) = E_l^{inc} + \int_\Omega k_0^2 \chi(\mathbf{r}') E_l(\mathbf{r}') G(\mathbf{r}, \prime) d\mathbf{r}', \tag{14}$$

where $\chi(\mathbf{r}) = \varepsilon_r(\mathbf{r}) - \varepsilon_{rb}$ denotes the permittivity contrast, $G(\mathbf{r}, \mathbf{r}')$ is the two dimensional homogeneous free space Green's function and k_0 represents the wave number in vacuum. For the sake of simplicity, the equations (13), (14) are rewritten using the operator notation, thus:

$$E_l^d = \mathbf{K}\chi E_l, \tag{15}$$

$$E_l = E_l^{inc} + \mathbf{G}\chi E_l, \tag{16}$$

The inverse scattering problem consists now in finding the function $\chi(\mathbf{r} \in \Omega)$ in the investigated area Ω (test domain) so that the diffracted field associated to χ matches the measured diffracted field $f_l(\mathbf{r} \in \Gamma)$. In the present section, we have limited the study to iterative approaches such as the Modified Gradient Method, referred to from now on as MGM.

The general principle of the MGM for solving this inverse scattering problem is to build up two sequences related to contrast and total field inside the test domain $\{\chi_n\}$ and $\{E_{l,n}\}$, respectively, according to the following recursive relations:

$$E_{l,n} = E_{l,n-1} + \alpha_{l,n} v_{l,n}, \tag{17}$$

$$\chi_n = \chi_{n-1} + \beta_n d_n, \tag{18}$$

where $v_{l,n}$ and d_n are search directions with respect to the total field $E_{l,n}$ and to the contrast, respectively. The choice of these search directions will be discussed in the next section. The coefficients $\alpha_{l,n}$ and β_n are weights that are chosen at each iteration step n so as to minimize the normalized cost functional $\mathcal{F}_n(\chi_n, E_{l,n})$ given by:

$$\begin{aligned}\mathcal{F}_n(\chi_n, E_{l,n}) &= \frac{\sum_{l=1}^{L} \left\| h_{l,n}^{(1)} \right\|_\Omega^2}{\sum_{l=1}^{L} \left\| E_l^{inc} \right\|_\Omega^2} + \frac{\sum_{l=1}^{L} \left\| h_{l,n}^{(2)} \right\|_\Gamma^2}{\sum_{l=1}^{L} \| f_l \|_\Gamma^2} \\ &= W_\Omega \sum_{l=1}^{L} \left\| h_{l,n}^{(1)} \right\|_\Omega^2 + W_\Gamma \sum_{l=1}^{L} \left\| h_{l,n}^{(2)} \right\|_\Gamma^2, \end{aligned} \tag{19}$$

where the normalizing coefficients W_Ω and W_Γ are as follows:

$$W_\Omega = \frac{1}{\sum_{l=1}^{L} \left\| E_l^{inc} \right\|_\Omega^2}, \qquad W_\Gamma = \frac{1}{\sum_{l=1}^{L} \left\| f_l \right\|_\Gamma^2}. \tag{20}$$

The subscripts Γ and Ω are included in the norm $\|\cdot\|$ and later in the inner product $<\cdot,\cdot>$ to indicate the domain of integration. The functions $h_{l,n}^{(1)}$ and $h_{l,n}^{(2)}$ are two residual errors. The first one is the residual error with respect to the incident field in the test domain computed from the field or coupling equation. The second residual error is the error on the scattered field computed from the state or observation equation.

$$h_{l,n}^{(1)} = E_l^{inc} - E_{l,n-1} + \mathbf{G}\chi_n E_{l,n}, \tag{21}$$

$$h_{l,n}^{(2)} = f_l - \mathbf{K}\chi_n E_{l,n}. \tag{22}$$

The use of *a priori* information may improve the inversion algorithm. For instance in [42] a binary constraint is used to reconstruct the shape of homogeneous object with known constitutive parameters and in [43] none-negative *a priori* information is applied to a pure imaginary contrasted object (conducting object) and in [44] non-negative *a priori* information is used to retrieve the shape of homogeneous object. We incorporated here *a priori* information stating that the real and imaginary parts of the scatterer's relative complex permittivity are non negative. Instead of retrieving a complex function χ_n, two real auxiliary functions ξ_n and η_n are reconstructed such that

$$\chi_n = 1 + \xi_n^2 + j\eta_n^2 - \varepsilon_{rb}, \tag{23}$$

wherein the real and imaginary parts of the relative complex permittivity distribution are forced to be greater than unity and non negative, respectively ($\Re e[\varepsilon_r] \geq 1$; $\Im m[\varepsilon_r] \geq 0$). The recursive relation with respect to contrast χ_n (18) is splitted into

$$\xi_n = \xi_{n-1} + \beta_{n;\xi} d_{n;\xi}, \tag{24}$$

$$\eta_n = \eta_{n-1} + \beta_{n;\eta} d_{n;\eta}. \tag{25}$$

Once the updating directions $d_{n;\xi}$, $d_{n;\eta}$ and $v_{l,n}$ are found, $\mathcal{F}_n$ is a nonlinear expression with L complex variables ($\alpha_{l,n;v}$) and two real

variables $(\beta_{n;\xi}, \beta_{n;\eta})$. The minimization of $\mathcal{F}_n$ is accomplished using the Polak-Ribière conjugate gradient method [45].

4.2 Search Directions

As updating directions $d_{n;\xi}$ and $d_{n;\eta}$, the authors take the standard Polak-Ribière conjugate gradient directions [43, 44].

$$d_{n;\xi} = g_{n;\xi} + \gamma_{n;\xi} d_{n-1;\xi} \text{ with } \gamma_{n;\xi} = \frac{< g_{n;\xi}, g_{n;\xi} - g_{n-1;\xi} >_\Omega}{\|g_{n-1;\xi}\|_\Omega^2}, \quad (26)$$

$$d_{n;\eta} = g_{n;\eta} + \gamma_{n;\eta} d_{n-1;\eta} \text{ with } \gamma_{n;\eta} = \frac{< g_{n;\eta}, g_{n;\eta} - g_{n-1;\eta} >_\Omega}{\|g_{n-1;\eta}\|_\Omega^2}, \quad (27)$$

where g_ξ and g_η are the gradients of the cost functional $\mathcal{F}_n(\xi, \eta, E_l)$ with respect to ξ and η respectively, evaluated at the $(n-1)$th step assuming that the total field inside the test domain does not change. These gradients are given by:

$$g_{n;\xi} = 2\xi_{n-1} \Re e \left[W_\Omega \sum_{l=1}^{L} \bar{E}_{l,n-1} \mathbf{G}^\dagger h_{l,n-1}^{(1)} - W_\Gamma \sum_{l=1}^{L} \bar{E}_{l,n-1} \mathbf{K}^\dagger h_{l,n-1}^{(2)} \right], \quad (28)$$

$$g_{n;\eta} = 2\eta_{n-1} \Im m \left[W_\Omega \sum_{l=1}^{L} \bar{E}_{l,n-1} \mathbf{G}^\dagger h_{l,n-1}^{(1)} - W_\Gamma \sum_{l=1}^{L} \bar{E}_{l,n-1} \mathbf{K}^\dagger h_{l,n-1}^{(2)} \right], \quad (29)$$

where the overbar denotes the complex conjugate, and $\mathbf{G}^\dagger$ and $\mathbf{K}^\dagger$ are the adjoint operators adjoint of $\mathbf{G}$ and $\mathbf{K}$, respectively.

The search direction $v_{l,n}$ for the total field inside the test domain is similar to those chosen for the object functions ξ and η.

$$v_{l,n} = g_{l,n;E} + \gamma_{l,n;E_l} v_{l,n-1} \quad \text{with} \quad \gamma_{l,n;E_l} = \frac{< g_{l,n;E_l}, g_{l,n;E_l} - g_{l,n-1;E_l} >_\Omega}{\|g_{l,n-1;E_l}\|_\Omega^2}, \quad (30)$$

where $g_{l,n;E_l}$ is the gradient of the cost functional $\mathcal{F}_n(\xi, \eta, E_l)$ with respect to the field E_l, evaluated at $(n-1)$th step and assuming that ξ and η do not change.

$$g_{l,n;E_l} = W_\Omega \left[\bar{\chi}_{n-1}\mathbf{G}^\dagger h^{(1)}_{l,n-1} - h^{(1)}_{l,n-1}\right] - W_\Gamma \bar{\chi}_l \mathbf{K}^\dagger h^{(2)}_{l,n-1}. \qquad (31)$$

Since a fast forward solver is available for the configuration concerned here [46], we added a second search direction $w_{l,n}$ for the total field inside the test domain; the recursive relation (17) with respect to the field E_l then becomes

$$E_{l,n} = E_{l,n-1} + \alpha_{l,n;v} v_{l,n} + \alpha_{l,n;w} w_{l,n}. \qquad (32)$$

The cost function $\mathcal{F}_n$ is now a nonlinear expression with $2L$ complex variables $(\alpha_{l,n;v}\,,\ \alpha_{l,n;w})$ and two real variables $(\beta_{n;\xi}\,,\ \beta_{n;\eta})$. The minimization of $\mathcal{F}_n$ is again accomplished using the Polak-Ribière conjugate gradient method [45].

The second updating direction for the total field $w_{j,n}$ is given by

$$w_{l,n} = \tilde{E}_{l,n-1} - E_{l,n-1}\ ; \qquad \tilde{E}_{l,n-1} = [1 - \mathbf{G}\chi_{n-1}]^{-1} E_l^{inc}, \qquad (33)$$

where $\tilde{E}_{l,n-1}$ represents the total field inside the test domain Ω, computed from the coupling equation with the contrast χ_{n-1}. Adding this search direction provided an acceleration of the algorithm's convergence at least in terms of number of iterations. Note that if $(\alpha_{l,n;v} = 0$ and $\alpha_{l,n;w} = 1)$ then $E_{l,n} = \tilde{E}_{l,n-1}$, in this case the scheme is a conjugate gradient algorithm, linearized method without a regularization procedure. Now, if $(\alpha_{l,n;v} \neq 0$ and $\alpha_{l,n;w} = 0)$ then $E_{l,n} = E_{l,n-1} + \alpha_{l,n;v} v_{l,n}$ which provides us with a standard modified gradient algorithm. Therefore, the algorithm presented above can be considered as a hybrid algorithm.

4.3 Initial Estimates: Backpropagation Technique

Given the *a priori* information stating that the objet functions ξ and η are positive, the initial guess $(\xi_0 = \eta_0 = 0)$ must be rejected since the gradients vanish $(g_{1;\xi} = g_{1;\eta} = 0)$. We therefore need another initial guess. This can be provided by the backpropagation method. We combined the initial guess obtained by backpropagation [44] relative to a real object function with the initial guess also obtained by backpropagation [43] relative to a pure imaginary object function. The process can be summarized in three steps:

1. **Estimation of $\zeta_{l,0} = \chi_0 E_{l,0}$:**

   Determination of a solution of the form

$$\zeta_{l,0} = \gamma_l \mathbf{K}^\dagger f_l \tag{34}$$

   with γ_l minimizing the cost function $\mathcal{F}(\gamma_j)$.

$$\mathcal{F}(\gamma_l) = \|f_l - \mathbf{K}\zeta_{l,0}\|_\Gamma^2 = \left\|f_l - \mathbf{K}\mathbf{K}^\dagger f_l\right\|_\Gamma^2. \tag{35}$$

   This parameter γ_l results from the necessary condition so that $\mathcal{F}(\gamma_l)$ is minimal

$$\gamma_l = \frac{< \mathbf{K}\mathbf{K}^\dagger f_l, f_l >_\Gamma}{\left\|\mathbf{K}\mathbf{K}^\dagger f_l\right\|_\Gamma^2}. \tag{36}$$

2. **Estimation of the total field $E_{l,0}$:**

   From $\zeta_{l,0}$ and using the field equation, we deduce an initial guess for the total field

$$E_{l,0} = E_l^{inc} + \mathbf{G}\zeta_{l,0} \tag{37}$$

3. **Estimation of objet functions ξ_0 and η_0:**

   From $\zeta_{l,0} = \chi_0 E_{l,0}$ and from the initial guess of the total field $E_{l,0}$ obtained above, we can deduce ξ_0 [44] and η_0 [43].

$$\xi_0^4(\mathbf{r} \in \Omega) = \frac{\displaystyle\sum_{l=1}^{L} \frac{\left\{\Re e\left[\zeta_{l,0}(\mathbf{r})\bar{E}_{l,0}(\mathbf{r}) + \varepsilon_{rb}|E_{l,0}(\mathbf{r})|^2 - |E_{l,0}(\mathbf{r})|^2\right]\right\}^2}{|E_{l,0}(\mathbf{r})|^2}}{\displaystyle\sum_{l=1}^{L} |E_{l,0}(\mathbf{r})|^2} \tag{38}$$

$$\eta_0^4(\mathbf{r} \in \Omega) = \frac{\displaystyle\sum_{l=1}^{L} \frac{\left\{\Im m\left[\zeta_{l,0}(\mathbf{r})\bar{E}_{l,0}(\mathbf{r}) + \varepsilon_{rb}|E_{l,0}(\mathbf{r})|^2\right]\right\}^2}{|E_{l,0}(\mathbf{r})|^2}}{\displaystyle\sum_{l=1}^{L} |E_{l,0}(\mathbf{r})|^2} \tag{39}$$

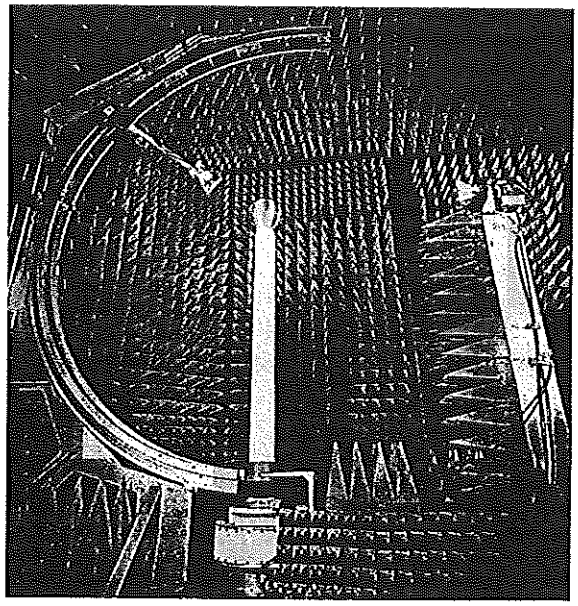

Figure 2. Experimental setup — anechoic chamber.

5. EXPERIMENTAL SETUP

5.1 Description

The experimental setup described here consists in an anechoic chamber, 14.2 m in length and 6.5 m both in width and height. It is designed to work in a frequency range from 300 MHz to 26.5 GHz. In addition, either the transmitter or the receiver can move along a circular line in the cross-sectional plane of the cylindrical target, allowing us to work with a bistatic configuration. The incidence and scattering angle are known with better accuracy than 0.5° . During our measurements, the transmitter was fixed, and the incidence angle was varied by rotating the scatterer around a vertical axis at the center of the setup (Fig. 2). This way, the incidence angle can vary from $-180°$ to $180°$. This is not the case of the scattering angle, since the encumbrance of the supports of the antennas prevents us to get angles smaller than 60° between the receiver and the transmitter.

The distances ρ_S and ρ_R , between the center of the experimental setup and the transmitter or the receiver, are 72.0 ± 0.3 cm and

76.8 ± 0.3 cm, respectively. To make the two-dimensional assumption realistic, the length of the targets in the direction of invariance was between 1 and 3 meters, in accordance with the directivity of the antennas, to make the incident field negligible at the ends of the scatterers. To cover of a wide frequency range with the same pair of antennas, wideband horn antennas, devoted to the $[1, 18]$ GHz range were used.

5.2 Incident Field

As mentioned above, the experimental setup uses wide band horn antennas. Their 3 dB bandwidth is quite large, from 30° at 1 GHz down to 15° at 16 GHz. Consequently, since the electric field is parallel to the cylinder axis at the input of the antenna, the field radiated in the vicinity of the cylinder is close to a TM cylindrical wave (magnetic field perpendicular to the cylinder axis). Therefore, the incident electric field is no longer parallel to the cylinder axis when moving away from the cross-section plane. From this point of view, the experiment is not achieved in a perfectly $E_{//}$ case of polarization. Writing the incident field as a superposition of plane waves would lead to conical diffraction problems, which couple TM and TE waves. However, bearing in mind that the cosine function decays slowly between 0 and 30° , and that the amplitude of the incident field decays very rapidly for higher angles, the deviation from the $E_{//}$ polarization remains small. In addition, the receiving antenna only measures the $E_{//}$ scattered field, thus does not take the cross-polarized component into account.

Except at $f = 1$ GHz, both emitting and receiving antennas are located at large distances compared to the wavelength as well as to the characteristic size of the target cross-section. For such a far-field configuration, it makes almost no difference to model the incident waves by plane waves or cylindrical isotropic ones. For reconstruction purposes, the complex amplitude of the modeled incident wave is estimated from the incident field measured in the forward direction. The Figures 3 and 4 display the measured and the calculated scattered field, respectively. The object is a metallic cylinder of rectangular cross-section and the numerical computation was achieved by a method based on a contour integral formalism [36] assuming that the object is perfectly conducting. The measured field agrees well with the calculated one and the normalized error

$$err = \frac{\sum_{l=1}^{36}\sum_{m=1}^{49}\left|E^{mes}(l,m) - E^{cal}(l,m)\right|^2}{\sum_{l=1}^{36}\sum_{m=1}^{49}|E^{cal}(l,m)|^2} \approx 0.055, \qquad (40)$$

where $E^{mes}(l,m)$ denote the measured scattered field at the mth receiver and for the lth position of emitting antenna. $E^{cal}(l,m)$ denotes the calculated field.

6. NUMERICAL RESULTS

6.1 Description of Targets and Data

In this section the authors present results of the reconstruction from experimental data using boundary and domain integral formalisms. Three different objects are reported and we refer the reader to the Table 1 to convert the sizes of the targets in terms of the wavelength in the vacuum. The data consist in measured real and imaginary parts of the scattered field (deduced by subtracting the incident field from the total field) at 49 different positions of the receiving antenna and for 36 different positions of the emitting antenna. The first example corresponds to a metallic cylinder of $(1.27 \times 2.54)\,\mathrm{cm}^2$ rectangular cross-section located at about $x = -0.5\,\mathrm{cm}$ and at about $-0.75\,\mathrm{cm}$ along the y-axis. The second example consists in a circular dielectric cylinder of radius $1.5\,\mathrm{cm}$ and of dielectric constant $\varepsilon_r = 3$. The cylinder is shifted from the center of the experimental setup along the y-axis, $y = 28\,\mathrm{mm}$. The third and last example corresponds to two identical circular dielectric cylinders of radius $1.5\,\mathrm{cm}$ and of dielectric constant $\varepsilon_r = 3$. One of the cylinder is located at about $x = 0$ and at $y = 4.5\,\mathrm{cm}$, while the other is located at about $x = -1.0\,\mathrm{cm}$ and at $y = -4.5\,\mathrm{cm}$. For the metallic cylinder the scattered field is collected for $f = 4\,\mathrm{GHz}$ and for $f = 16\,\mathrm{GHz}$. The scattered field for the circular dielectric is carried out for $f = 2\,\mathrm{GHz}$ and for $f = 8\,\mathrm{GHz}$. For the last example, two dielectric cylinders, the scattered field has been measured for $f = 1\,\mathrm{GHz}$ and for $f = 4\,\mathrm{GHz}$.

Table 1. Wavelength in free space at the chosen operating frequencies.

f [GHz]	λ [cm]
1	30
4	7.5
8	3.75
16	1.88

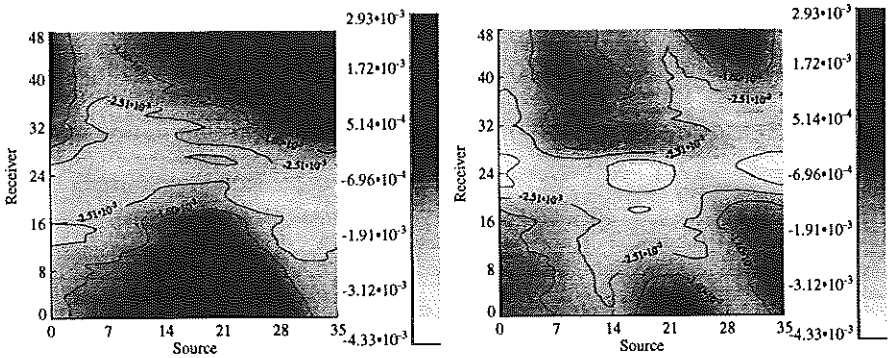

Figure 3. Real and imaginary parts of the measured scattered field by metallic cylinder with rectangular cross-section sized $(1.27 \times 2.54)\,\mathrm{cm}^2$ at $f = 4\,\mathrm{GHz}$. The correction of the incident field has been taken into account.

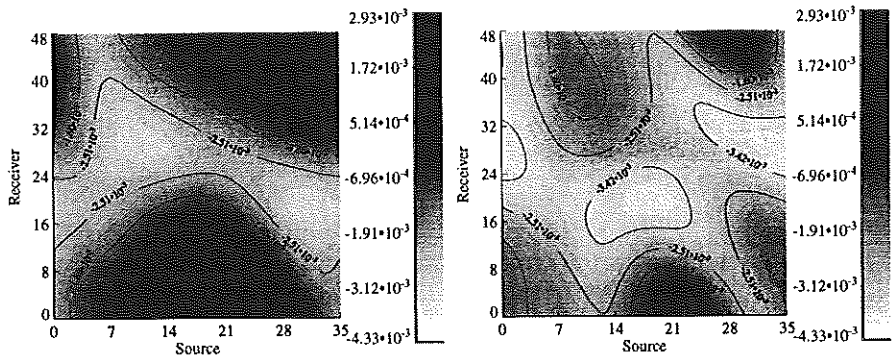

Figure 4. Real and imaginary parts of the calculated scattered field by perfectly conducting cylinder of rectangular cross-section sized $(1.27 \times 2.54)\,\mathrm{cm}^2$ at $f = 4\,\mathrm{GHz}$. The metallic cylinder is located at $x = -0.5\,\mathrm{cm}$ and at $y = -0.75\,\mathrm{cm}$.

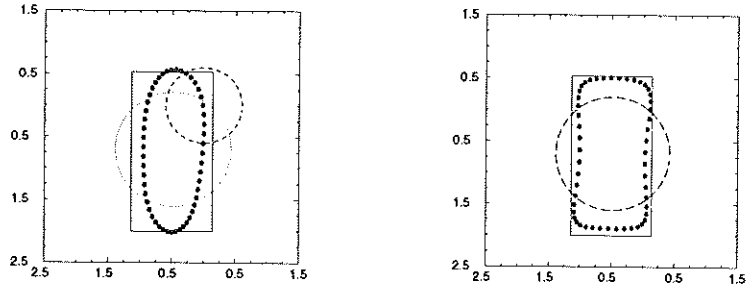

Figure 5. Reconstructed boundary of the metallic cylinder at $f = 4\,\mathrm{GHz}$ (left) and at $f = 16\,\mathrm{GHz}$ (right). The bold dotted curve represents the final result for each operating frequency and the solid line represents the actual shape of the object to be retrieved. At $f = 4$ GHz the dashed line represents the initial guess deduced from DORT method combined with the low frequency approximation, the plain dotted line presents the optimal circle. At $f = 16$ GHz the dashed line corresponds to the initial guess which is the optimal circle found at $f = 4$ GHz. The object has been assumed to be perfectly conducting only to generate the initial estimate and the reconstructed conductivity at $f = 4$ GHz and $f = 16\,\mathrm{GHz}$ is $\sigma = 51\,\mathrm{S/m}$, $\sigma = 11\,\mathrm{S/m}$, respectively.

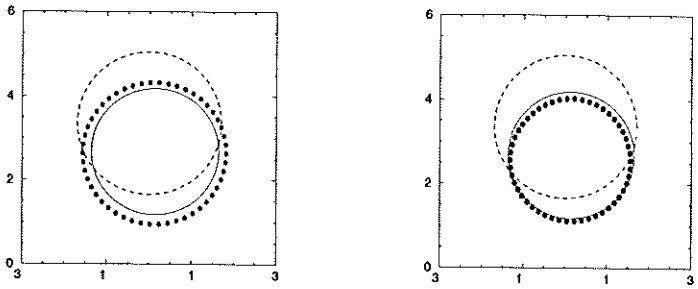

Figure 6. Reconstructed boundary of the circular dielectric cylinder at $f = 2\,\mathrm{GHz}$ (left) and at $f = 8\,\mathrm{GHz}$ (right). The bold dotted curve represents the final result for each operating frequency and the solid line represents the actual shape of the object to be retrieved. At $f = 2\,\mathrm{GHz}$ the dashed line represents the initial guess deduced from DORT method combined with the low frequency approximation. At $f = 8\,\mathrm{GHz}$ the dashed line corresponds to the initial guess found at $f = 2\,\mathrm{GHz}$. The dielectric constant used to generate the initial estimate is $\varepsilon_r = 1$ and the reconstructed relative permittivity is $\varepsilon_r = 2.95$ and $\varepsilon_r = 3.89$ at $f = 2\,\mathrm{GHz}$ and $f = 8\,\mathrm{GHz}$, respectively.

6.2 Boundary Method

The reconstructions performed with the boundary integral method result from a multi-frequency approach. Indeed, the higher the frequency, the harder the convergence of the inversion algorithm to achieve. Since our initial guess is based on a low frequency approximation, inversion in the resonance domain requires two steps. This is illustrated with the reconstruction of the metallic rectangular rod. At $f = 4\,\mathrm{GHz}$, the area of the cross-section is about $\lambda/3 \times \lambda/6 \simeq \lambda^2/18$. In this range, the low frequency approximation is still accurate and, assuming an infinite conductivity, leads to the initial guess plotted as a circular dotted line in Fig. 5. Then, following the regularization process, an optimal circle, very well centered on the actual scatterer is found after fifteen iterations. This circle has been used as initial guess for reconstructions at higher frequencies. As shown in Fig. 5, it allows the algorithm to converge at $f = 16\,\mathrm{GHz}$ (about 200 iterations), when the cross-section area is about one wavelength square. Though expected, the improvement of the resolution from 4 to 16 GHz is to be noticed. Concerning conductivity, the inversion leads to 51 S/m at $f = 4\,\mathrm{GHz}$ and to 11 S/m at $f = 16\,\mathrm{GHz}$, both corresponding to a skin depth close to 0.1 cm. The next example concerns the single circular dielectric rod. Since our regularization scheme consists in truncating the Fourier series describing the boundary, stabilization of the cost function is achieved much more rapidly when reconstructing a circle than a rectangle. This is why the number of iterations here is twice or three times smaller than previously. Starting from $f = 2\,\mathrm{GHz}$ (Fig. 6), a low frequency approximation provides an initial guess which also allows convergence at higher frequencies. As an example, the reconstruction at $f = 8\,\mathrm{GHz}$ is given in Fig. 6. The result may not seem impressive because of the circular shape of the boundary, but it must be kept in mind that this information is not known *a priori*, and that the number of Fourier coefficients to optimize was not restricted to one. As a result, the boundary is very well reconstructed, while the permittivity is over estimated, $\varepsilon_r = 3.9$ to be compared to the measured value $\varepsilon_r = 3.0$ obtained from a technique using waveguides [47]. On the contrary, at $f = 2\,\mathrm{GHz}$, the permittivity was well estimated $\varepsilon_r = 2.95$, but the radius of the reconstructed circle was too large. It is interesting to notice that, whatever the frequency, at the end of the reconstruction process, the product of the cross-section area by the contrast of permittivity is always the same. This is a typical

ambiguity of the low frequency range, which may drive the algorithm to local minima. A more significant example is given next. Let us consider two identical dielectric rods, similar to the previous one, separated by a distance $d = 9\,\text{cm}$ between their centers, and let us start our study at $f = 1\,\text{GHz}$. Unfortunately, at this frequency it was not possible for us to separate the rods from the initial guess. Therefore, starting from a single circular rod (dashed line in Fig. 7), the reconstruction leads to a single scatterer, much larger than the actual rods, but with smaller permittivity $\varepsilon_r = 1.4$, such that the product of the contrast of permittivity by the cross-section area is correct, in accordance with low frequency approximations. This shortcoming does not occur at $f = 4\,\text{GHz}$ where the DORT method provides two isolated scatterers lying in the investigated area, located at the centers of the dashed circles plotted in Fig. 7. As initial guess, two circles with arbitrary radii (but small enough for the boundaries not to cross during the reconstruction) and permittivity of vacuum have been chosen. In this case, the reconstruction is quite accurate in terms of locations, sizes and permittivities ($\varepsilon_r = 3.42$ and 3.46 instead of 3). On the other hand, since the scattered field no longer mirrors the symmetry of revolution of the cylinders, the reconstruction is not as accurate as for one circular body.

6.3 Domain Method

The initial guesses for the reconstructions with MGM are all obtained by backpropagation technique and all the final results reported here correspond to the 16th iteration for which the cost function reached a plateau. Moreover, the reconstructions have been performed in two steps according to the multi-frequency approach. We start the reconstruction at the lowest available operating frequency with very large square test domain of size $(20 \times 20)\,\text{cm}^2$ and we reduce the investigated domain for the reconstruction at higher frequency. For the metallic cylinder, at the lower frequency $f = 4\,\text{GHz}$, the test domain Ω consists in a large square domain of surface about $7\lambda^2$ and the complex relative permittivity (object function) is discretized into 30×30 equal subsquare cells. The real part of the reconstructed complex permittivity distribution is found more or less homogeneous inside Ω and its value is close to unity. Therefore only the reconstructed conductivity distribution is presented in Fig. 8. The final value of the cost function is $F_{16} = 0.07$ and the maximum of the reconstructed conduc-

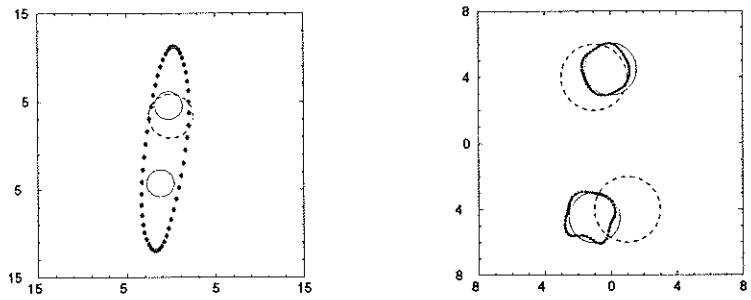

Figure 7. Reconstructed boundary of two circular dielectric cylinders at $f = 1\,\text{GHz}$ (left) and at $f = 4\,\text{GHz}$ (right). The bold dotted curve represents the final result for each operating frequency and the solid lines represent the actual shapes of the objects to be retrieved. The dashed lines represent the initial guesses. The dielectric constant used to generate the initial estimates is $\varepsilon_r = 1$ and the reconstructed relative permittivity is $\varepsilon_r = 1.4$ at $f = 1\,\text{GHz}$. At $f = 4\,\text{GHz}$ the reconstructed relative permittivities are $\varepsilon_r = 3.42$ and $\varepsilon_r = 3.46$ for the upper and the lower cylinder, respectively.

tivity is $\sigma_{\max} = 2.7\,\text{S/m}$ which corresponds to a skin depth of $0.5\,\text{cm}$. From the reconstruction at $f = 4\,\text{GHz}$, one can observe that the unknown object is included in a rectangular subdomain plotted in dashed line in Fig. 8. This rectangular subdomain is used for the reconstruction at the higher frequency $f = 16$ GHz for which the test domain has been changed as well as its discretization. For this frequency the investigated domain Ω consists now in a rectangular domain of size $(2.5\times 5)\,\text{cm}^2 \approx 0.22\lambda^2$ centered at $x = -0.5\,\text{cm}$ and $y = -7.5\,\text{cm}$. The object function to be retrieved is discretized into 20×40 equal subsquare cells. The reconstructed conductivity distribution is presented in Fig. 8 and the maximum value of the conductivity is $\sigma_{\max} = 4.8\,\text{S/m}$ correspondingto a skin depth of $0.2\,\text{cm}$. The final cost function value is $F_{16} = 0.10$. The reconstruction is clearly improved when switching the frequency. For the second example, the reconstruction of the circular dielectric cylinder at the lower frequency $f = 2\,\text{GHz}$ has been performed with a square test domain of the same size as the one used for the reconstruction at $f = 4\,\text{GHz}$ of the metallic cylinder. The reconstructed conductivity distribution vanishes inside Ω and therefore only the reconstructed real part of the complex relative permittivity

distribution is presented in Fig. 9 and the maximum value of the reconstructed permittivity is $\varepsilon_r = 4.2$, which is quite large compared to the actual one $\varepsilon_r = 3$. The final value of the cost function is $F_{16} = 0.007$. The dashed square box of Fig. 9, sized $(5 \times 5)\,\mathrm{cm}^2$ represents the new investigated domain Ω that is used for the reconstruction at higher frequency $f = 8\,\mathrm{GHz}$. The result of the reconstruction is presented in Fig. 9 and the maximum value of the reconstructed permittivity is now $\varepsilon_r = 3.6$ instead of 4.2 previously. The final value of the cost function at $f = 8$ GHz is $F_{16} = 0.04$. The Fig. 10 compares the actual relative permittivity with the reconstructed one along a diameter of the cylinder. The cylinder has been correctly located with a good estimate of the shape as well as of its constitutive material. For the last example, corresponding to two identical circular cylinders, the result of the inversion at the lower frequency $f = 1\,\mathrm{GHz}$ with the large test domain is presented in Fig. 11. The final value of the cost function is $F_{16} = 0.02$. The low frequency result doesn't show that two distinct objects are present inside Ω, but the reconstructed permittivity distribution differs from the background permittivity in a rectangular subdomain centered at the center of the experimental setup (dashed box in Fig. 11). The rectangular domain is used as investigated domain for the reconstruction at $f = 8\,\mathrm{GHz}$. The size of the test domain is now $(8.5 \times 17)\,\mathrm{cm}^2 \approx 2.6\lambda^2$ and it is discretized into 20×40 equal subsquare cells. The result is presented in Fig. 11 and now the two cylinders are detected. The final value of the cost function is $F_{16} = 0.02$. Fig. 12 presents a comparison between the actual dielectric constant and the reconstructed one along diameters of the circular cylinders.

Inversions from real data performed with boundary and domain integral formalism lead to very close results especially for the dielectric cases. For the conducting object the reconstructed shapes are similar, but the reconstructed conductivity is higher with the boundary method. The authors presented results of reconstructions in the case of $E_{//}$ polarization, however satisfactory results have been obtained with $H_{//}$ polarization using the boundary method. Full results are reported in [48]. Data described in this paper as well as in [48] are at disposal of anyone interested.

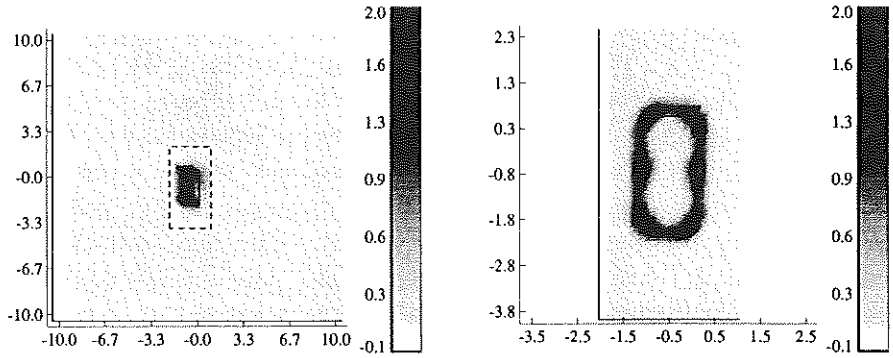

Figure 8. Map of the conductivity distribution reconstructed with the MGM for the metallic cylinder of rectangular cross-section at $f = 16\,\text{GHz}$ (right) and at $f = 4\,\text{GHz}$ (left). The dashed rectangular box is used as investigated domain for the inversion at $f = 16\,\text{GHz}$. The solid line represents the actual shape.

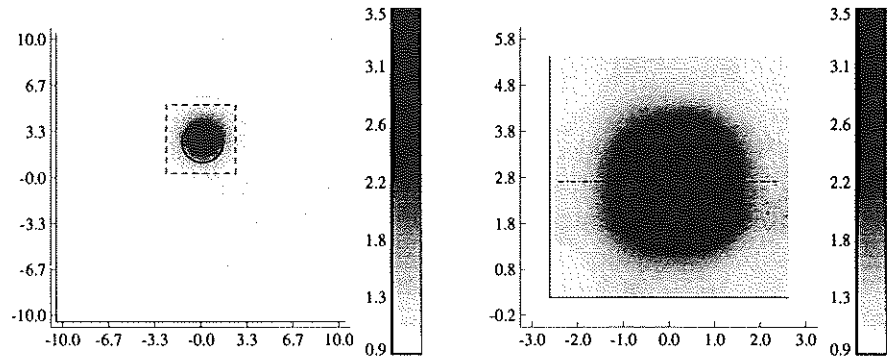

Figure 9. Reconstructed real part of the relative complex permittivity distribution with the MGM for the single circular dielectric cylinder at $f = 2\,\text{GHz}$ (left) and at $f = 8\,\text{GHz}$ (right). The dashed square box is used as the test domain for the reconstruction at $f = 8$ GHz. The solid circle represents the actual shape. A comparison between the actual permittivity and the reconstructed one along the dash-dotted line is presented in Fig. 10.

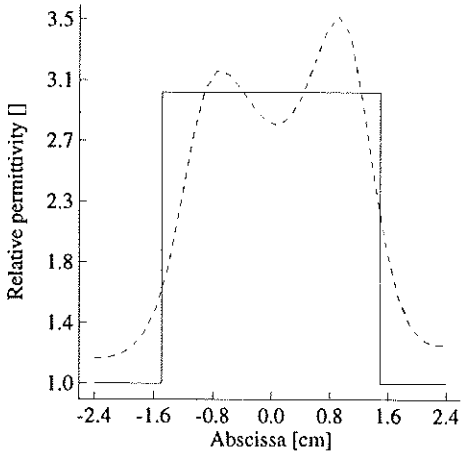

Figure 10. Cross-sectional cut along the dash-dotted line plotted in Fig. 9. Solid and dashed line, respectively, present the measured relative permittivity and the reconstructed relative permittivity at $f = 8\,\mathrm{GHz}$.

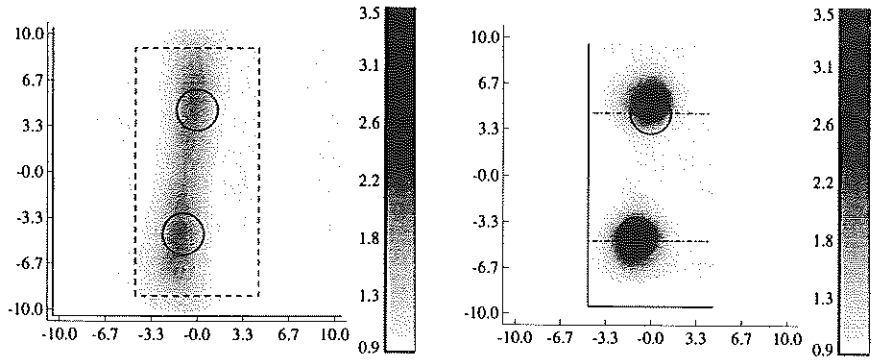

Figure 11. Reconstructed real part of the relative complex permittivity distribution with MGM for the example corresponding to two identical circular dielectric cylinders at $f = 1\,\mathrm{GHz}$ (left) and at $f = 8\,\mathrm{GHz}$ (right). The solid line circles represent the actual shapes and the dashed rectangular box represents the investigated domain that is used for the reconstruction at $f = 8\,\mathrm{GHz}$. A comparison between the actual permittivities and the reconstructed ones along the dash-dotted lines is shown in Fig. 12.

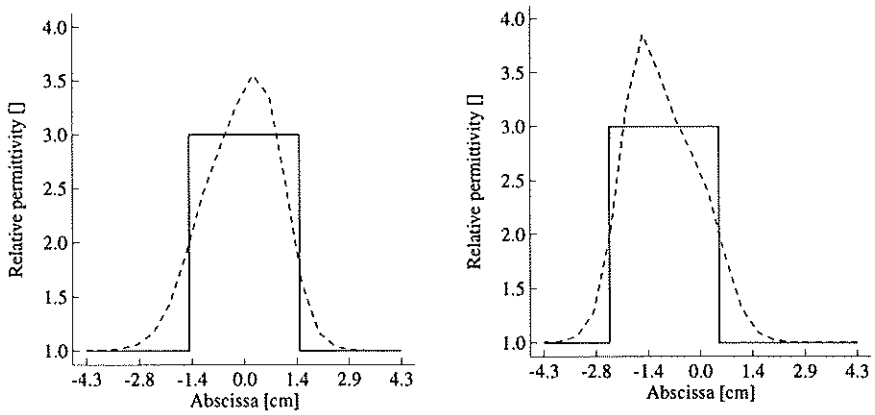

Figure 12. Cross-sectional cut along the dash-dotted lines plotted in Fig. 11. Solid and dashed line, respectively, present the measured relative permittivity and the reconstructed relative permittivity at $f =$ 8 GHz. The left graph corresponds to the upper cylinder of Fig. 11 and the right graph corresponds to the lower cylinder of Fig. 11.

7. CONCLUSION

In this paper, both the experimental setup and reconstruction algorithms have been validated. We have presented two different inverse reconstruction methods. One is based on the contour integral formalism which is particularly adapted to reconstructing the shape and permittivity of homogeneous objects. The second method is based on domain integral formalism and retrieves complex permittivity distribution. Both methods succeeded in reconstructing dielectric and conducting objects. The dynamic range of the setup has allowed us to accurately measure the field scattered by a small dielectric rod in a bistatic configuration.

Multi-frequency data can be recorded with wide band horn antennas. This is very useful for reconstructions in the resonance domain where convergence often requires an initial guess rather close to the solution. Indeed, since the algorithms are more robust in the lower frequency range, such an initial guess can be derived from a rough reconstruction at low frequency. This technique has been successfully used here with both domain and boundary methods.

These results encourage us to now deal with more complicated targets, like inhomogeneous cylinders. In addition, since the experimen-

tal setup is also designed for three-dimensional bistatic measurements, three-dimensional objects can be investigated if algorithms are available.

REFERENCES

1. Devaney, A. J., "Geophysical diffraction tomography," *IEEE Trans. Geosc. Remote Sensing*, Vol. 22, 3–13, 1984.
2. Bolomey, J. C., and C. Pichot, "Microwave tomography: from theory to practical imaging systems," *Int. J. Imaging Syst. Technol.*, Vol. 2, 144–156, 1990.
3. Roger, A., "Newton-Kantorovitch algorithm applied to an electromagnetic inverse problem," *IEEE Transactions on Antennas and Propagation*, Vol. 29, No. 2, 232–238, 1981.
4. Tijhuis, A. G., "Born-type reconstruction of material parameters of an inhomogeneous lossy dielectric slab from reflected-field data," *Wave Motion*, Vol. 11, 151–173, 1989.
5. Chew, W. C., and Y. M. Wang, "Reconstruction of two-dimensional permittivity distribution using distorted Born iterative method," *IEEE Trans. Med. Imaging*, Vol. 9, 218–225, 1990.
6. Kleinman, R. E., and P. M. van den Berg, "A modified gradient method for two-dimensional problems in tomography," *Journal of Computational and Applied Mathematics*, Vol. 42, 17–35, 1992.
7. van den Berg, P. M., and R. E. Kleinman, "A contrast source inversion method," *Inverse Problems*, Vol. 13, 1607–1620, 1997.
8. Colton and Kress, *Inverse Acoustic and Electromagnetic Scattering Theory*, Berlin, Springer-Verlag, 1992.
9. McGahan, R. V., and R. E. Kleinman, "Special session on image reconstruction using real data," *IEEE Antennas and Propagation Magazine*, Vol. 38, No. 3, 39–40, 1996.
10. Belkebir, K., J. M. Elissalt, J. M. Geffrin, and C. Pichot, "Newton-Kantorovich and modified gradient inversion algorithms applied to Ipswich data," *IEEE Antennas and Propagation Magazine*, Vol. 38, No. 3, 41–44, 1996.
11. Duchêne, B., and D. Lesselier D., "On modified-gradient solution methods using the binary aspect of the unknown electromagnetic parameters and their application to the Ipswich data," *IEEE Antennas and Propagation Magazine*, Vol. 38, No. 3, 45–47, 1996.
12. Lobel, P., R. E. Kleinman, C. Pichot, L. Blanc-Féraud, and M. Barlaud, "Conjugate-gradient method for solving inverse scattering with experimental data," *IEEE Antennas and Propagation Magazine*, Vol. 38, No. 3, 48–51, 1996.

13. Lu, C. C., and W. C. Chew, "Processing Ipswich data with local shape function method," *IEEE Antennas and Propagation Magazine*, Vol. 38, No. 3, 51–53, 1996.
14. Morris, J. B., D. A. Pommet, R. V. McGahan, and M. A. Friddy, "Imaging of unknown targets from measured scattering data," *IEEE Antennas and Propagation Magazine*, Vol. 38, No. 3, 53–56, 1996.
15. van den Berg, P. M., and R. E. Kleinman, "Image reconstruction from Ipswich data," *IEEE Antennas and Propagation Magazine*, Vol. 38, No. 3, 56–59, 1996.
16. McGahan, R. V., and R. E. Kleinman, "Second annual special session on image reconstruction using real data," *IEEE Antennas and Propagation Magazine*, Vol. 39, No. 2, 7–8, 1997.
17. Duchêne, B., D. Lesselier, and R. E. Kleinman, "Inversion of the 1996 Ipswich data using binary specialization methods," *IEEE Antennas and Propagation Magazine*, Vol. 39, No. 2, 9–12, 1997.
18. Lobel, P., C. Pichot, L. Blanc-Féraud, and M. Barlaud, "Conjugate-gradient algorithm with edge-preserving regularization for image reconstruction from Ipswich data for mystery objects," *IEEE Antennas and Propagation Magazine*, Vol. 39, No. 2, 12–14, 1997.
19. Maponi, P., L. Misici, and F. Zirilli, "A numerical method to solve the inverse medium problem: an application to the Ipswich data," *IEEE Antennas and Propagation Magazine*, Vol. 39, No. 2, 14–19, 1997.
20. Pommet, D., R. A. Marr, U. H. W. Lammers, R. V. McGahan, J. B. Morris, and M. A. Fiddy, "Imaging using limited-angle backscattered data from real targets," *IEEE Antennas and Propagation Magazine*, Vol. 39, No. 2, 19–22, 1997.
21. Morris, J. B., R. V. McGahan, J. L. Shmitz, R. M. Wing, D. A. Pommet, and M. A. Fiddy, "Imaging of strongly-scattering targets from real data," *IEEE Antennas and Propagation Magazine*, Vol. 39, No. 2, 22–26, 1997.
22. Murch, R. D., and D. G. H. Tan, "Reconstructing objects from the Ipswich data set," *IEEE Antennas and Propagation Magazine*, Vol. 39, No. 2, 26–28, 1997.
23. van den Berg, P. M., B. J. Kooij, and R. E. Kleinman, "Image reconstruction from Ipswich data II," *IEEE Antennas and Propagation Magazine*, Vol. 39, No. 2, 29–32, 1997.
24. McGahan, R. V., and R. E. Kleinman, "The third annual special session on image reconstruction using real data, part 1," *IEEE Antennas and Propagation Magazine*, Vol. 41, No. 1, 34–36, 1999.

25. Marr, R. A., D. A. Pommet, U. H. W. Lammers, R. V. McGahan, and M. A. Fiddy, 'Target recognition from limited-angle backscatter," *IEEE Antennas and Propagation Magazine*, Vol. 41, No. 1, 36–40, 1999.
26. Pommet, D. A., J. B. Morris, R. V. McGahan, and M. A. Fiddy, "Imaging of unknown targets measured scattering data," *IEEE Antennas and Propagation Magazine*, Vol. 41, No. 1, 40–44, 1999.
27. Maponi, F., and F. Zirilli, "A numerical method to solve the inverse medium problem: an application to the Ipswich data II," *IEEE Antennas and Propagation Magazine*, Vol. 41, No. 1, 44–47, 1999.
28. Lobel, P., Pichot C., Blanc-Féraud L., Barlaud M., and Louis A. K. image reconstruction from the 1997 Ipswich data using a conjugate-gradient algorithm. *IEEE Antennas and Propagation Magazine*, Vol. 41, No. 1, 48–51, 1999.
29. Crosta, G. F., "The third annual special session on image reconstruction using real data, part 2. The application of back-propagation algorithms to the Ipswich data: Preliminary results," *IEEE Antennas and Propagation Magazine*, Vol. 41, No. 2, 20–26, 1999.
30. van den Berg, P. M., B. J. Kooij, and R. E. Kleinman, "Image reconstruction from Ipswich data — III," *IEEE Antennas and Propagation Magazine*, Vol. 41, No. 2, 27–32, 1999.
31. Rieger, W., M. Haas, G. Lehner, and W. M. Rucker, "Image reconstruction from real scattering data using an iterative scheme with incorporated a priori information," *IEEE Antennas and Propagation Magazine*, Vol. 41, No. 2, 33–40, 1999.
32. Kleinman, R. E., and P. M. van den Berg, "An extended range-modified gradient technique for profile inversion," *Radio Science*, Vol. 28, No. 5, 877–884, 1993.
33. Aarts, A., and J. Korst, *Numerical Recipes. Simulated Annealing and Boltzmann Machines*, Wiley & Sons (Eds.), New York, 1989.
34. Chew, W. C., and J. H. Lin, "A frequency-hopping approach for microwave imaging of large inhomogeneous bodies," *IEEE Microwave and Guided Wave Letters*, Vol. 5, No. 12.
35. Belkebir, K., and A. G. Tijhuis, "Using multiple frequency information in the iterative solution of two-dimensional nonlinear problem," *Proc. Progress in Electromagnetic Research Symposium (Innsbruck)*, 353, 1996.
36. Saillard, M., P. Vincent, and D. Maystre, *A Finite Element Method for Electromagnetic Subsurface Tomography*, 237–265, T. Itoh, G. Pelosi, P. Silvester, (Eds.), Wiley J. & Sons, New York, 1996.

37. Roger, A., "Reciprocity theorem applied to the computation of functional derivatives of the scattering matrix," *Electromagnetics*, Vol. 2, 69–83, 1982.
38. Bonnard, S., P. Vincent, and M. Saillard, "Cross-borehole inverse scattering using a boundary finite-element method," *Inverse Problems*, Vol. 14, 521–534, 1998.
39. Prada, C., and M. Fink, "Eigenmodes of the time reversal operator: a solution to selective focusing in multiple-target media," *Wave Motion*, Vol. 20, 151–163, 1994.
40. Bouchal, Z., and J. Perina, "Electromagnetic concept of phase conjugation," *Journal of Modern Optics*, Vol. 45, 425–436, 1998.
41. Tortel, H., G. Micolau, and M. Saillard, "Decomposition of the time reversal operator for electromagnetic scattering," *Journal of Electromagnetic Waves and Applications*, Vol. 13, 687–719, 1999.
42. Souriau, L., B. Duchêne, D. Lesselier, and R. E. Kleinman, "Modified gradient approach to inverse scattering for binary objects in stratified media," *Inverse Problems*, Vol. 12, 463–481, 1996.
43. Kleinman, R. E., and P. M. van den Berg, "Two-dimensional location and shape reconstruction," *Radio Science*, Vol. 29, No. 4, 1157–1169, 1994.
44. Belkebir, K., R. E. Kleinman, and C. Pichot, "Microwave imaging — Location and shape reconstruction from multifrequency scattering data," *IEEE Transactions on Microwave Theory and Techniques*, Vol. 45, No. 4, 469–476, 1997.
45. Press, W. H., B. P. Flannery, S. A. Teukolski, and W. T. Vetterling, *Numerical Recipes. The Art of Scientific Computing*, Cambridge University Press, 1986.
46. Peng, Z. Q., and A. G. Tijhuis, "Transient scattering by a lossy dielectric cylinder: marching-on-in-frequency approach," *Journal of Electromagnetic Waves and Applications*, Vol. 7, No. 5, 739–763, 1993.
47. Weir, W. B., "Automatic measurement of complex dielectric constant and permeability at microwave frequencies," *Proceedings of IEEE*, Vol. 62, No. 1, 33–36, 1974.
48. Bonnard, S., *Reconstruction d'objets homogènes bidimensionnels en électromagnétisme: application à la tomographie*, Ph.D. thesis, Université d'Aix-Marseille III, 1999.

Kamal Belkebir was born in Algeria in 1966. He received the Ph.D. degree in Physics from the University of Paris XI (Orsay), France in 1994. He worked from 1995 to 1997 at the University of Eindhoven, the Netherlands on Post-doctoral position. He joined the Laboratoire d'Optique Electromagnétique in 1997 and he is currently "Maître de

Conférences" at the University of Provence in Marseille. His research deals with both forward and inverse scattering techniques.

Stéphane Bonnard was born in Aubenas on March 30, 1972. He received the Engineering degree in 1995 from the Ecole Nationale Supérieure de Physique, Marseille, and the Ph.D. degree in 1999 from University of Aix-Marseille, France. His area of research was about electromagnetic inverse problems.

Frederic Pezin was born in Lille, France, in 1969. He received the Ph.D. degree in Physics in 1998 from the University of Lille, France. He worked during his Ph.D. thesis on electromagnetic compatibility problems, mainly on the Mode Stirred Reverberating Chambers. Since 1998, he is employed by the National Center for Scientific Research (CNRS) as Research Engineer at the Laboratoire d'Optique Electromagnétique in Marseille. He is involved in RCS measurements, Near and Far field radiation pattern and spherical near field radiation pattern of antennas. His research interest include also the RF facilities characterization by using numerical electromagnetic.

Pierre Sabouroux was born in Clermont-Ferrand, France, in 1966. He received the Ph.D. degree in Physics in 1992 from the University of Bordeaux, France. He worked during his Ph.D. thesis on new techniques of characterization of dielectric materials. He is presently Maître de Conférences at the University of Provence. He is in charge of an anechoïc chamber at the Laboratoire d'Optique Electromagnétique in Marseille where different techniques are used to measure RCS of particular targets and to measure near and far field radiation pattern (targets or antennas) in planar or spherical geometries.

Marc Saillard received the Ph.D. degree in Physics from the University of Aix-Marseille, France, in 1990. From 1990 to 1997, he was a researcher at the National Center for Scientific Research (CNRS) associated with the Laboratoire d'Optique Electromagnétique in Marseille. He is presently a Professor at the University of Provence in Marseille, and is managing the Remote Sensing and Microwave Applications team of the Fresnel Institute. His current research interests include inverse scattering, remote sensing and wave propagation in random media and rough surfaces. Pr Saillard is a member of the Electromagnetic academy.